Physica B 685 (2024) 415995

Contents lists available at ScienceDirect

Physica B: Condensed Matter

journal homepage: www.elsevier.com/locate/physb

Temperature-dependent local structure and lattice dynamics of 1T-$TiSe_2$ and 1T-VSe_2 probed by X-ray absorption spectroscopy

Inga Pudza [a], Boris Polyakov [a], Kaspars Pudzs [a], Edmund Welter [b], Alexei Kuzmin [a,*]

[a] Institute of Solid State Physics, University of Latvia, Kengaraga street 8, LV-1063 Riga, Latvia
[b] Deutsches Elektronen-Synchrotron DESY, Notkestr. 85, 22607 Hamburg, Germany

ARTICLE INFO

Keywords:
Transition metal dichalcogenides
Interlayer and intralayer coupling
Extended X-ray absorption fine structure
Reverse Monte Carlo simulations
Effective force constants

ABSTRACT

The local atomic structure and lattice dynamics of two isostructural layered transition metal dichalcogenides (TMDs), 1T-$TiSe_2$ and 1T-VSe_2, were studied using temperature-dependent X-ray absorption spectroscopy at the Ti, V, and Se K-edges. Analysis of the extended X-ray absorption fine structure (EXAFS) spectra, employing reverse Monte Carlo (RMC) simulations, enabled tracking of the temperature evolution of the local environment in the range of 10–300 K. The atomic coordinates derived from the final atomic configurations obtained using the RMC method were used to calculate the partial radial distribution functions (RDFs) and the mean-square relative displacement (MSRD) factors for the first ten coordination shells around the absorbing atoms. Characteristic Einstein frequencies and effective force constants were determined for Ti–Se, Ti–Ti, V–Se, V–V, and Se–Se atom pairs from the temperature dependencies of MSRDs. The obtained results reveal differences in the temperature evolution of lattice dynamics and the strengths of intralayer and interlayer interactions in $TiSe_2$ and VSe_2.

1. Introduction

Transition metal dichalcogenides (TMDs) have garnered significant attention in the scientific community due to their layered structure, resulting in remarkable electronic, optical, mechanical, tribological, catalytic, and magnetic properties as well as numerous possible technological applications [1–4]. Among all, the charge density wave (CDW) behavior observed for a number of TMDs MX_2 (M = Ti, V, Ta; X = S, Se) is particularly fascinating [5–7]. Indeed, TMDs represent the first layered materials in which the presence of CDWs was detected [8]. The CDW state involves the periodic modulation of the electron density within the material coupled with lattice distortion, leading to changes in the material electronic and optical properties [9,10]. Models describing CDW mechanisms are based solely on crystal structure distortion/superlattice formation, exciton–phonon interactions, or electron–phonon interactions [11,12]. Due to the minute nature of distortion or atomic shifts in the CDW state (~0.1–0.15 Å), the resulting superstructure might generate only relatively faint secondary peaks within the X-ray diffraction patterns [10].

In this paper, two isostructural TMDs, namely titanium selenide ($TiSe_2$) and vanadium selenides (VSe_2), were selected to evaluate the effect of the CDW ordering on their local environments. The choice of TMDs was dictated by the feasibility of measuring high-quality X-ray absorption spectra at both the metal and chalcogenide K absorption edges.

Under ambient conditions, both $TiSe_2$ and VSe_2 crystallize in the 1T polytype with a space group of $P\bar{3}m1$ (164) (Fig. 1) [13,14]. In this structure, the Ti(V) atoms are octahedrally coordinated to six covalently bonded Se atoms, and [Ti(V)Se_6] octahedra are connected by edges into layers, joined by weak van der Waals (vdW) interactions. The interactions between neighboring layers play an important role in assembling and exfoliation of vdW (hetero)structures and, thus, allow engineering of their electronic, optical, and mechanical properties [15–17]. While the importance of weak interlayer coupling is recognized, its accurate experimental quantification remains challenging [16,18].

A commensurate CDW phase in bulk 1T-$TiSe_2$ forms below $T_{CDW} \approx$ 202 K with a $2a \times 2a \times 2c$ superlattice [11,19]. The neutron diffraction study proposed the low-temperature (at 77 K) lattice distortion due to displacements of about 0.085 Å for Ti and 0.028 Å for Se parallel to the plane of the layer [19]. However, more recent synchrotron X-ray scattering experiments pointed to a zone-boundary phonon softening mechanism of CDW in 1T-$TiSe_2$ [20,21].

1T-VSe_2 undergoes an incommensurate CDW transition at $T_{CDW} \approx$ 110 K and a commensurate CDW transition at ≈80 K, forming a $4a \times 4a \times 3c$ superlattice [22,23]. The origin of the CDW in VSe_2 was

* Corresponding author.
E-mail addresses: inga.pudza@cfi.lu.lv (I. Pudza), boris.polyakov@cfi.lu.lv (B. Polyakov), kaspars.pudzs@cfi.lu.lv (K. Pudzs), edmund.welter@desy.de (E. Welter), a.kuzmin@cfi.lu.lv (A. Kuzmin).

https://doi.org/10.1016/j.physb.2024.415995
Received 30 December 2023; Received in revised form 26 March 2024; Accepted 19 April 2024
Available online 22 April 2024
0921-4526/© 2024 Elsevier B.V. All rights reserved.

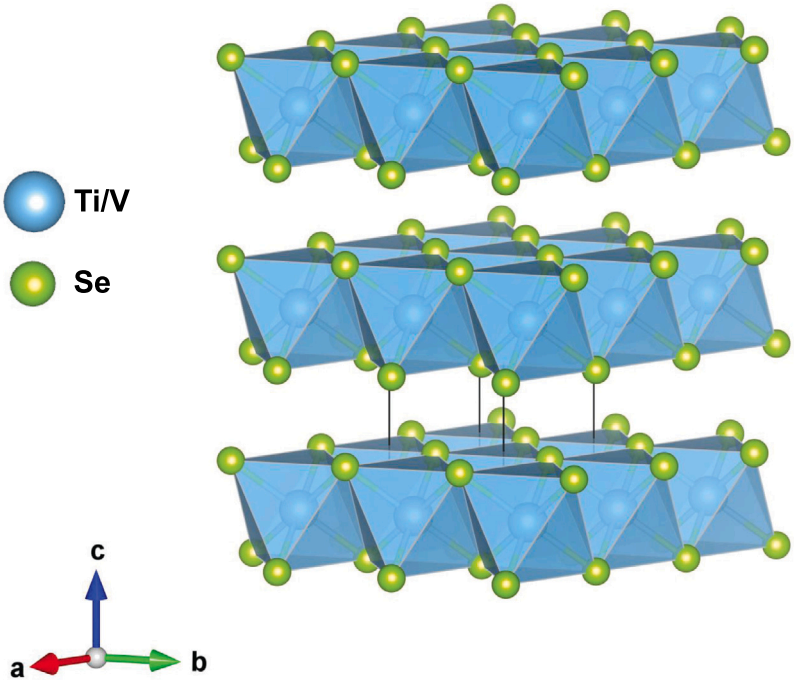

Fig. 1. Crystallographic structure of trigonal (space group $P\bar{3}m1$ (164)) $TiSe_2$ (VSe_2) [13,14].

attributed to the electron–phonon interaction, based on inelastic X-ray scattering and first-principles calculations [24]. Besides, an important role of vdW forces in the CDW melting was proposed, likely caused by the out-of-plane nature of the CDW, which modulates interlayer distance [24]. Recently, a pressure-induced CDW state was observed in VSe_2 at room temperature within the pressure range of 10–15 GPa by Raman spectroscopy [25] and X-ray diffraction (XRD) [10]. The Se K-edge X-ray absorption spectroscopy (XAS) was also used in [10] to probe local distortions but only qualitative analysis was reported.

In this study, we employed XAS combined with the advanced data analysis methodology of extended X-ray absorption fine structure (EXAFS), based on reverse Monte Carlo (RMC) simulations coupled with an evolutionary algorithm (EA) approach [26,27], to investigate the local atomic structure and lattice dynamics in bulk 1T-$TiSe_2$ and 1T-VSe_2.

The RMC method was originally proposed more than 30 years ago by McGreevy and Pusztai [28] to determine a three-dimensional model of the atomic structure of disordered systems that is consistent with the experimentally measured structure factor or the obtained radial distribution function. Two years latter, it was first used for the analysis of EXAFS spectra by Gurman and McGreevy [29]. In recent years, the RMC method has gradually gained popularity due to its ability to properly incorporate thermal and static disorder effects in multiple-scattering EXAFS calculations, easily introduce different constraints provided by other experimental techniques, and account for EXAFS spectra measured at multiple absorption edges [30–33]. Further details on the strengths and weaknesses of the method can be found in a recent review [34].

We have demonstrated recently [18] that employing the RMC method for 2H_c-MoS_2 enables the retrieval of structural data from distant coordination shells and, thus, provides valuable information on both interlayer and intralayer coupling. Here we took advantage of high-quality EXAFS spectra measured at two (Ti/V and Se) K absorption edges and performed their simultaneous analysis to reconstruct the temperature evolution of the local environment in the corresponding TMDs in the range of 10–300 K. This allowed us to determine the amplitudes of thermal vibrations for atoms located in the first ten coordination shells around absorbing atoms, which were further used to evaluate the strengths of interlayer and intralayer interactions. We showed that despite the isostructural nature of $TiSe_2$ and VSe_2, the temperature-dependent evolution of their lattice dynamics has some peculiarities.

2. Materials and methods

2.1. Synthesis procedure

$TiSe_2$ and VSe_2 were prepared using the chemical vapor transport technique with an I_2 transport agent [35,36]. The starting materials titanium (or vanadium) and selenium in the form of powder were weighed out with a molar ratio of M:Se = 1:2 (M = Ti or V) and loaded into a quartz ampoule together with the iodine (molar ratio I_2:M = 0.05). The filled ampoule was evacuated to pressure 10^{-5} torr and sealed at a length of approximately 12–14 cm using the oxygen-methane flame. For $TiSe_2$ synthesis the ampoule was heated in a two-zone furnace with T_{hot} = 700 °C at the hot zone and T_{cold} = 600 °C at the cold zone for 24 h, then naturally cooled down (for VSe_2 T_{hot} = 820 °C, T_{coldt} = 650 °C, heating time 72 h).

2.2. X-ray diffraction

The phase purity of the TMD samples was confirmed using X-ray powder diffraction (XRD). Diffraction patterns were collected at room temperature using a benchtop Rigaku MiniFlex 600 diffractometer with Bragg–Brentano θ–2θ geometry. An X-ray tube with copper anode (Cu Kα radiation, λ = 1.5418 Å), operated at U = 40 kV and I = 15 mA, was used as a source. The obtained X-ray diffraction patterns of $TiSe_2$ and VSe_2 are compared in Fig. 2 with the reference ones. All Bragg peaks were indexed to pure $TiSe_2$ (PDF Card 04-003-1758) and VSe_2 (PDF Card 01-074-1411) phases possessing $P\bar{3}m1$ (164) space group. Slight variations in peak intensities are noticeable, likely attributed to the favored alignment of layered structures that could arise during the process of sample preparation. No impurity phases were detected, demonstrating the single-phase composition of the synthesized samples.

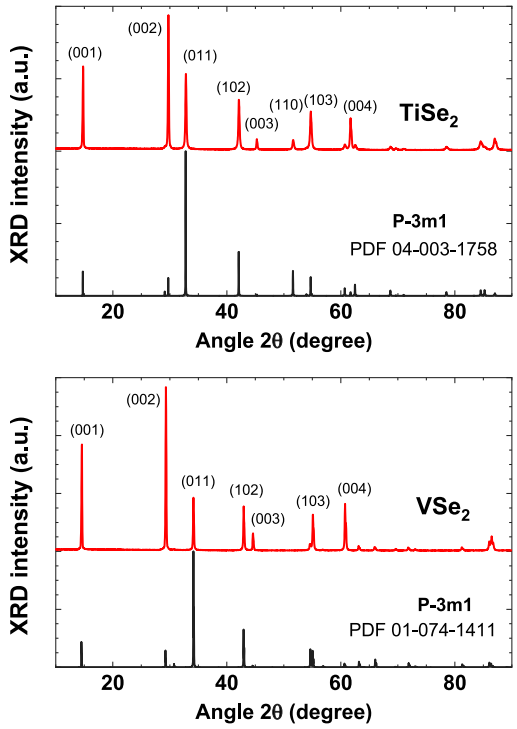

Fig. 2. Powder X-ray diffraction patterns of synthesized 1T-$TiSe_2$ and 1T-VSe_2. Main Bragg peaks are indexed to the $P\bar{3}m1$ (164) space group. Reference patterns corresponding to $TiSe_2$ (PDF Card 04-003-1758) and VSe_2 (PDF Card 01-074-1411) phases are shown for comparison.

2.3. X-ray absorption experiments

The temperature-dependent (10–300 K) X-ray absorption spectra of bulk 1T-$TiSe_2$ and 1T-VSe_2 were recorded at Ti (4966 eV), V (5465 eV) and Se (12658 eV) K-edges in transmission mode at the DESY PETRA III P65 Applied XAFS undulator beamline [37]. The storage ring operated in top-up 480 bunch mode at the energy E = 6.08 GeV and current I = 100 mA. The synchrotron radiation was monochromatized using a Si(111) double-crystal monochromator, and its intensity before and after the sample was measured by two ionization chambers. The harmonic rejection was achieved by the uncoated silicon plane mirror.

Experimental Ti, V and Se K-edge EXAFS spectra were extracted following the conventional procedure [38] using the XAESA code [39]. The EXAFS spectra $\chi(k)k^2$ and their Fourier transforms (FTs) are shown at selected temperatures in Fig. 3. Note that the FTs were not adjusted to compensate for the backscattering phase shift of atoms, therefore, the positions of all peaks appear shifted towards shorter distances compared to their crystallographic values.

2.4. Reverse Monte Carlo simulations

The structural information encoded in the experimental EXAFS spectra was extracted using the reverse Monte Carlo (RMC) method based on an evolutionary algorithm (EA) approach implemented in the EvAX code [26,27]. The RMC/EA-EXAFS technique aims to minimize the discrepancy between the experimental and calculated EXAFS spectra. As a result, it enables the reconstruction of the three-dimensional structural model of the material by introducing random atomic displacements within specific geometric constraints [26,27].

In this study, the initial structural models for the RMC/EA calculations were constructed based on diffraction data [13,14]. $TiSe_2$ and VSe_2 crystallize in the space group $P\bar{3}m1$ (164) with the lattice parameters $a = b$ = 3.540 Å, c = 6.008 Å for $TiSe_2$ [13] and $a = b$ = 3.355 Å, c = 6.134 Å for VSe_2 [14]. A supercell with a size of $6a\times6b\times4c$, including 432 atoms, and periodic boundary conditions was constructed for both compounds. During the RMC calculations, the size and shape of the supercell were fixed, and the number of atoms in the supercell was constant. At each iteration, all atoms in the supercell were displaced with the maximum allowed displacement set to 0.4 Å. As a result of such small displacements, the coordination numbers were held constant throughout the calculation. 32 atomic configurations were employed simultaneously in the EA method [27].

The configuration-averaged EXAFS spectra at the Ti/V and Se K-edges were calculated using the ab initio self-consistent real-space multiple-scattering FEFF8.5L code [40,41] taking into account multiple-scattering contributions up to the 5th order. The complex energy-dependent exchange–correlation Hedin-Lundqvist potential was employed to account for inelastic effects [42]. The values of the non-structural parameters, such as E_0 and S_0^2 [38], were determined by performing simulations for the highest-quality experimental data (the EXAFS spectra measured at 10 K) to achieve optimal alignment and minimize residuals in the wavelet transform space. Subsequently, the amplitude scaling parameter S_0^2 was set to 0.9 (for Ti K-edge) or 1.0 (for V and Se K-edges) and remained fixed for the entire series of experimental data, albeit potentially introducing some systematic errors. Multiple RMC calculations were conducted at each temperature using different sequences of pseudo-random numbers to estimate statistical dispersion. The mean-square relative displacement (MSRD) factors σ^2 for the first ten coordination shells around the absorbing atoms were calculated using the median absolute deviation (MAD) method [43,44]. The deviation between the smallest and largest MSRD values obtained from these calculations is comparable to the effect resulting from adjusting S_0^2 by ±0.1.

The structural model was adjusted in each RMC/EA calculation by minimizing the difference between the Morlet wavelet transforms (WTs) [45] of the experimental and calculated EXAFS spectra at two absorption edges (Ti and Se for $TiSe_2$ or V and Se for VSe_2) simultaneously. As a result, good agreement between the experimental and configuration-averaged EXAFS spectra was achieved in both the direct (R) and reciprocal (k) space.

An example of fits at the selected temperatures is shown in Fig. 4. The convergence of each RMC/EA simulation was attained after 3000 iterations. To improve statistics, seven independent RMC/EA calculations were carried out for each experimental data set, employing distinct sequences of pseudo-random numbers. The agreement between the configuration-averaged EXAFS spectra and the experimental data at all temperatures affirms the reliability of the obtained structural models. The calculated partial contributions of single-scattering and combined multiple-scattering paths to the total EXAFS spectra $\chi(k)k^2$ at 10 K are shown in Fig. 5. Note that the total number of single- and multiple-scattering paths included in the analysis was up to 1200, with those having a distance difference of less than 0.5 Å grouped together in the RMC calculations.

The atomic coordinates derived from the final RMC/EA configurations were utilized to calculate the partial radial distribution functions (RDFs) and to obtain relevant structural parameters. The MSRD factors σ^2 for Ti–Se, Ti–Ti, V–Se, V–V, and Se–Se atom pairs, which account for the thermal and static disorder, were calculated using the MAD method for the first ten coordination shells [43,44].

The temperature dependencies of the obtained MSRDs, $\sigma^2(T)$, were approximated using the correlated Einstein model [46]

$$\sigma^2(T) = \sigma_{st}^2 + (\hbar/2\mu\omega_E)\coth(\hbar\omega_E/2k_BT) \quad (1)$$

where σ_{st}^2 is the static contribution, μ is the reduced mass of the atomic pair, ω_E is the characteristic Einstein frequency, and k_B is the Boltzmann constant. The Einstein frequency ω_E can be used to determine the effective force constant $\kappa = \mu\omega_E^2$ [47], which is a useful parameter for estimating and comparing the strength of interatomic interactions. The values of the characteristic Einstein frequencies ω_E and the effective force constants κ for the relevant atomic pairs are reported in Tables 1 and 2. The uncertainties reported in the tables correspond to standard errors of the fits.

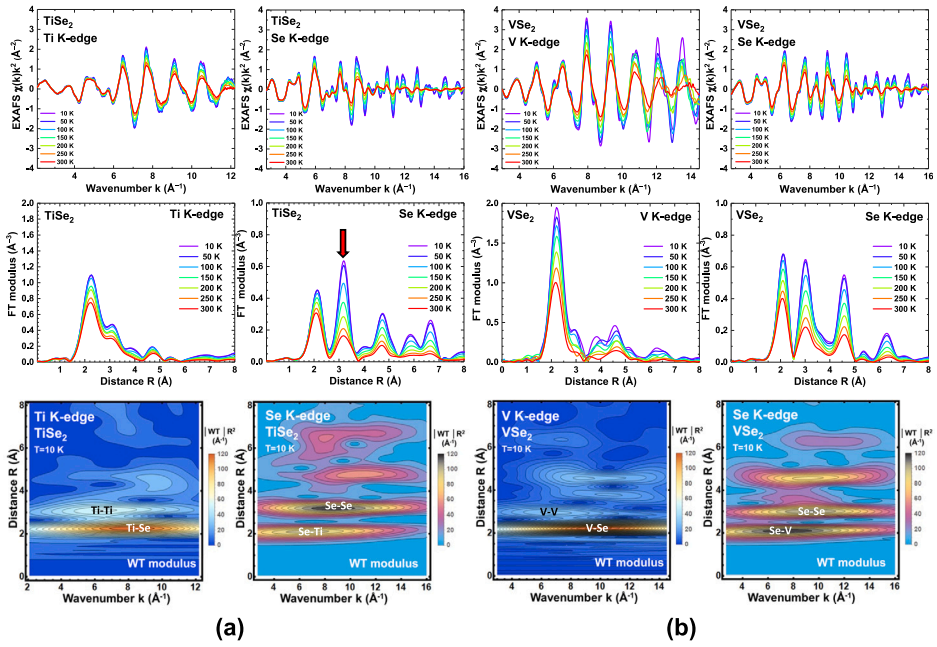

Fig. 3. Temperature-dependent EXAFS spectra $\chi(k)k^2$ (top panels), their Fourier transforms (only modulus is shown) (middle panels) and wavelet transforms at 10 K (bottom panels) for $TiSe_2$ (a) and VSe_2 (b).

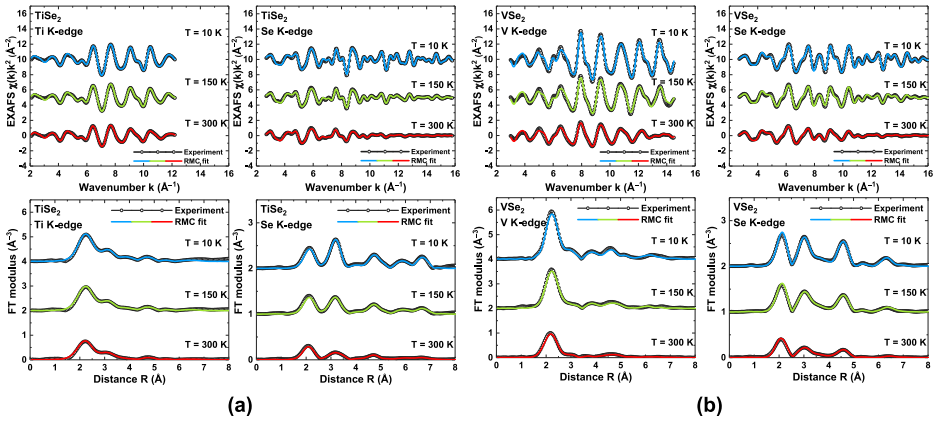

Fig. 4. Results of the RMC/EA calculations for the Ti and Se K-edges in $TiSe_2$ (a) and V and Se K-edges in VSe_2 (b) at selected (10, 150 and 300 K) temperatures. The EXAFS spectra $\chi(k)k^2$ are displayed within their respective fitting ranges. The fitting R-space ranges were 1.5–5.9 Å (Ti K-edge) and 1.2–7.1 Å (Se K-edge) for $TiSe_2$ and 1.0–7.0 Å (V K-edge) and 1.2–7.5 Å (Se K-edge) for VSe_2.

3. Results and discussion

The crystallographic structure of $TiSe_2$ (VSe_2) (Fig. 1) consists of a titanium (vanadium) atomic layer sandwiched between two selenium atomic layers [13,14]. These layers are weakly bonded to each other along the c-axis through vdW forces. The interlayer gap between Se atoms is about 3.12 Å in $TiSe_2$ and 3.16 Å in VSe_2. Ti(V) atoms are covalently bonded to six selenium atoms, forming regular octahedra. The values of Ti–Se, Ti–Ti, and Se–Se interatomic distances for the first ten coordination shells in $TiSe_2$ are reported in Table 1, while the values of V–Se, V–V, and Se–Se interatomic distances in VSe_2 are summarized in Table 2.

Despite the similarity between the two crystallographic structures, a notable difference can be observed as well. In the case of VSe_2, the interatomic distances between selenium atoms along the c-axis direction within the same layer and across adjacent layers coincide ($r_{Se_0-Se^{**}_{3/4}}$ = 3.63 Å), adding complexity to the analysis. In contrast, in $TiSe_2$, the Se^*_3 atoms in the adjacent layer are approximately 0.1 Å closer to the absorbing Se_0 than the Se_4 atoms within the same layer, so the two interatomic distances are different $r_{Se_0-Se^*_3}$ = 3.58 Å and $r_{Se_0-Se_4}$ = 3.68 Å.

The Ti K-edge EXAFS spectra of $TiSe_2$ and their FTs are dominated by a contribution from the first two coordination shells at all studied temperatures in the range of 10–300 K (Fig. 3(a)). These coordination shells consist of six selenium and six titanium atoms, respectively. The complex pattern of WTs observed at longer distances is attributed to outer shells and multiple-scattering effects. Note that heavier Se atoms with an atomic mass of 78.971 amu produce a greater impact on the EXAFS spectra at larger k values, whereas lighter Ti elements with an atomic mass of 47.867 amu contribute at lower k-values.

The Se K-edge EXAFS spectra of $TiSe_2$ contain contributions from scattering paths that extend beyond ~7 Å as evident in the FTs and WTs in Fig. 3(a). Their analysis can yield novel insights into the interactions between layers [18]. Indeed, the second peak at about 3.2 Å in FTs (indicated with a red arrow in Fig. 3(a)) contains contributions from intralayer ($r_{Se_0-Se_2}$ = 3.54 Å, $r_{Se_0-Se_4}$ = 3.68 Å) and interlayer ($r_{Se_0-Se^*_3}$ = 3.58 Å) selenium atoms, and its amplitude becomes significantly suppressed upon sample heating. Note that the amplitude of other peaks

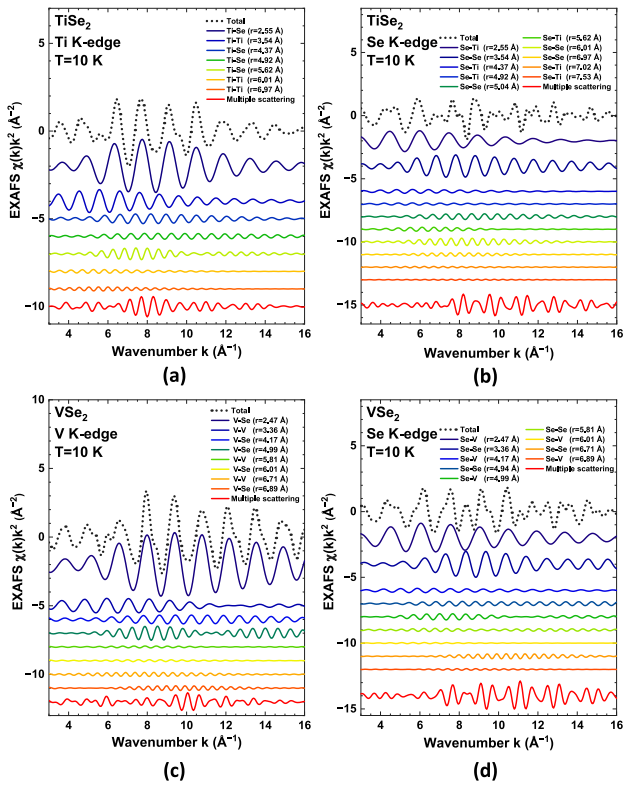

Fig. 5. Example of the calculated partial contributions (solid curves) of single-scattering and combined multiple-scattering paths to the total (dotted curves) EXAFS spectra at the Ti(Se) K-edges in $TiSe_2$ (a, b) and V(Se) K-edges in VSe_2 (c, d) at 10 K. The effective distances of the single-scattering paths are given in brackets.

Table 1
Values of coordination numbers (N) and Ti–Se, Ti–Ti, and Se–Se interatomic distances r for the first ten coordination shells of Ti and Se calculated from the crystallographic structure of $TiSe_2$ [13]. Interlayer distances are marked with "*". The values of characteristic Einstein frequencies (ω_E) and the effective force constants (κ) obtained from the RMC/EA analysis are also given for each atom pair.

Atom pair	N	Distance r (Å)	ω_E (THz)	κ (N/m)
Ti_0–Se_1	6	2.55	32.3 ± 0.4	51.61 ± 0.01
Ti_0–Ti_2	6	3.54	31.3 ± 0.6	39.02 ± 0.02
Ti_0–Se_3	6	4.37	23.3 ± 0.4	26.92 ± 0.01
Ti_0–Se_4^*	6	4.92	23.3 ± 0.6	26.94 ± 0.02
Ti_0–Se_5	12	5.62	25.6 ± 0.9	32.43 ± 0.04
Ti_0–Ti_6^*	2	6.01	25.6 ± 1.7	25.99 ± 0.12
Ti_0–Se_7^*	6	6.06	26.8 ± 1.2	35.65 ± 0.07
Ti_0–Ti_8	6	6.13	32.4 ± 0.6	41.69 ± 0.01
Ti_0–Ti_9^*	12	6.97	29.8 ± 1.9	35.41 ± 0.14
Ti_0–Se_{10}^*	12	7.02	26.2 ± 0.2	33.96 ± 0.01
Se_0–Ti_1	3	2.55	32.3 ± 0.4	51.61 ± 0.01
Se_0–Se_2	6	3.54	20.7 ± 0.2	28.12 ± 0.01
Se_0–Se_3^*	3	3.58	28.1 ± 1.2	51.95 ± 0.10
Se_0–Se_4	3	3.68	31.7 ± 1.3	65.81 ± 0.12
Se_0–Ti_5	3	4.37	23.3 ± 0.4	26.92 ± 0.01
Se_0–Ti_6^*	3	4.92	23.3 ± 0.6	26.94 ± 0.02
Se_0–Se_7^*	3	5.04	22.4 ± 0.5	32.89 ± 0.02
Se_0–Se_8	3	5.11	24.7 ± 0.6	39.96 ± 0.03
Se_0–Ti_9	6	5.62	25.6 ± 0.9	32.43 ± 0.04
Se_0–Se_{10}^*	2	6.01	24.6 ± 0.8	39.53 ± 0.04

up to ~7 Å is also reduced upon increasing thermal disorder but the peaks remain distinguishable even at 300 K.

While the reliable analysis of distant coordination shells is challenging within the conventional EXAFS methodology [38], it can be performed using the RMC/EA method [18,27,48]. Examples of the RMC/EA simulations of the Ti and Se K-edge EXAFS spectra for $TiSe_2$ at three selected temperatures (10, 150 and 300 K) are shown in Fig. 4

Table 2
Values of coordination numbers (N) and V–Se, V–V, and Se–Se interatomic distances r for the first ten coordination shells of V and Se calculated from the crystallographic structure of VSe_2 [14]. Interlayer distances are marked with "*". Coordination shells composed of both intralayer and interlayer atomic pairs are marked with "**". The values of characteristic Einstein frequencies (ω_E) and the effective force constants (κ) obtained from the RMC/EA analysis are also reported for each atom pair.

Atom pair	N	Distance r (Å)	ω_E (THz)	κ (N/m)
V_0–Se_1	6	2.47	31.1 ± 0.8	49.69 ± 0.04
V_0–V_2	6	3.36	16.6 ± 0.4	11.67 ± 0.01
V_0–Se_3	6	4.17	21.7 ± 0.4	24.25 ± 0.01
V_0–Se_4^*	6	4.99	24.9 ± 1.0	31.84 ± 0.06
V_0–Se_5	12	5.35	21.3 ± 0.6	23.23 ± 0.02
V_0–V_6	6	5.81	29.5 ± 2.3	36.81 ± 0.22
V_0–Se_7^*	6	6.01	25.4 ± 1.6	33.13 ± 0.13
V_0–V_8^*	2	6.13	28.4 ± 1.3	34.03 ± 0.07
V_0–V_9	6	6.71	20.1 ± 1.2	17.16 ± 0.06
V_0–Se_{10}^*	12	6.89	26.2 ± 1.1	35.22 ± 0.06
Se_0–V_1	3	2.47	31.1 ± 0.8	49.69 ± 0.04
Se_0–Se_2	6	3.36	24.5 ± 0.4	39.32 ± 0.01
Se_0–$Se_{3/4}^{**}$	3+3	3.63	27.1 ± 1.4	48.18 ± 0.12
Se_0–V_5	3	4.17	21.7 ± 0.4	24.25 ± 0.01
Se_0–$Se_{6/7}^{**}$	3+3	4.94	25.1 ± 0.6	41.19 ± 0.02
Se_0–V_8	3	4.99	24.9 ± 1.0	31.84 ± 0.06
Se_0–V_9	6	5.35	21.3 ± 0.6	23.23 ± 0.02
Se_0–Se_{10}	6	5.81	23.5 ± 0.4	36.16 ± 0.01

in k- and R-space. Good agreement between experimental and calculated EXAFS spectra is observed, enabling a comprehensive analysis of thermal disorder effects within the first ten coordination shells up to about 6 Å.

Different partial contributions due to single-scattering and combined multiple-scattering paths to the total EXAFS spectra $\chi(k)k^2$ of $TiSe_2$ and VSe_2 at 10 K are compared in Fig. 5. As expected, the strongest contributions come from the nearest shells. At the Ti and V K-edges, the first shell dominates, while the next four shells around Ti and three shells around V also exhibit large amplitudes. In the case of Se, the first and second shells dominate, while the amplitudes of other shells are relatively smaller. Note that the combined multiple-scattering contributions are important at all three absorption edges.

The coordinates of atoms derived from the RMC/EA simulations were employed to calculate the partial RDFs $g(r)$ (Fig. 6) and the MSRDs σ^2 (Fig. 7) for Ti–Ti, Ti–Se(Se–Ti), and Se–Se atom pairs at each temperature. The temperature dependencies of the obtained MSRDs $\sigma^2(T)$ in the range of 10–300 K were further approximated using the correlated Einstein model [46]. As a result, the characteristic Einstein frequencies ω_E and the effective force constants κ were obtained for all coordination shells and are reported in Table 1.

The effective force constants κ for the first two coordination shells of titanium (Ti_0–Se_1 and Ti_0–Ti_2) are about 52 N/m and 39 N/m, respectively, suggesting strong interaction between the nearest atoms. The interactions between absorbing Ti_0 and the next Se atoms located in the same (Se_3) or in the adjacent layer (Se_4^*) are close, as indicated by similar values of $\kappa \approx 27$ N/m. At the same time, the intralayer Ti–Ti interactions (Ti_0–Ti_2, Ti_0–Ti_8) are slightly stronger ($\kappa \approx$ 39–42 N/m) than the interlayer Ti–Ti interactions (Ti_0–Ti_6^*, Ti_0–Ti_9^*) with $\kappa \approx$ 26–35 N/m. Among all Se–Se atom pairs, the interaction between the nearest selenium atoms is the weakest ($\kappa_{Se_0-Se_2} \approx 28$ N/m), while the interaction between two selenium atoms located at opposite sides of the same layer is more than twice stronger ($\kappa_{Se_0-Se_4} \approx 66$ N/m). At the same time, the interaction between selenium atoms in adjacent layers across the vdW gap is rather strong with $\kappa_{Se_0-Se_3^*} \approx 52$ N/m. To conclude, the temperature dependencies of the MSRD factors in $TiSe_2$ do not show any unusual behavior.

In spite of the similarities in the crystallographic structures of $TiSe_2$ and VSe_2, the EXAFS spectra $\chi(k)k^2$ of VSe_2 have stronger amplitude and, as a result, more intense peaks in FTs (Fig. 3). The V K-edge EXAFS spectra of VSe_2, their FTs and WTs (Fig. 3(b)) are dominated by a

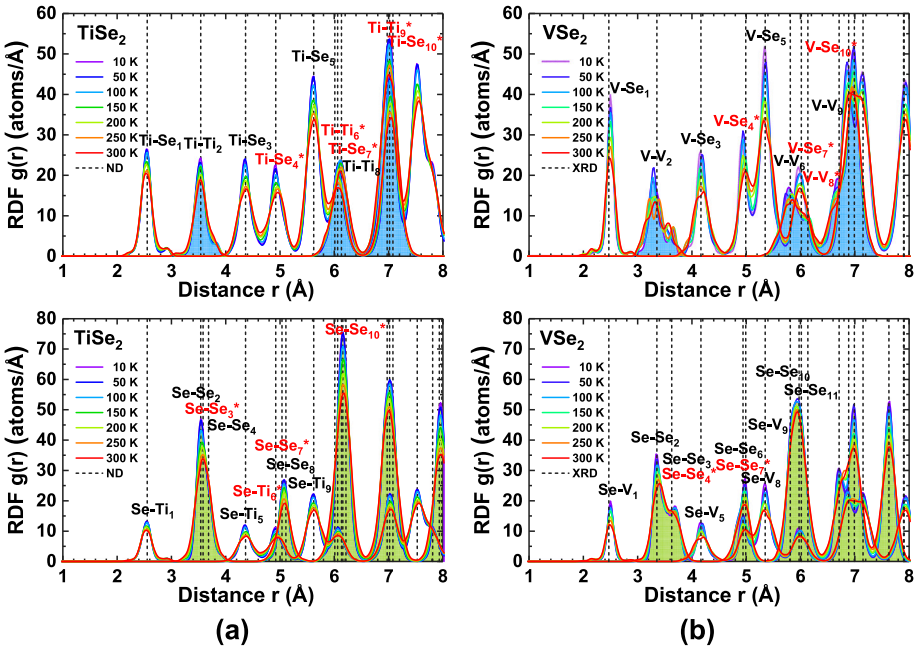

Fig. 6. Partial radial distribution functions (RDFs) around Ti and Se atoms in $TiSe_2$ (a) and V and Se atoms in VSe_2 (b) as a function of temperature. Open and filled peaks correspond to different partial RDFs. Vertical dashed lines are used to show the interatomic distances estimated from diffraction at room temperature [13,14].

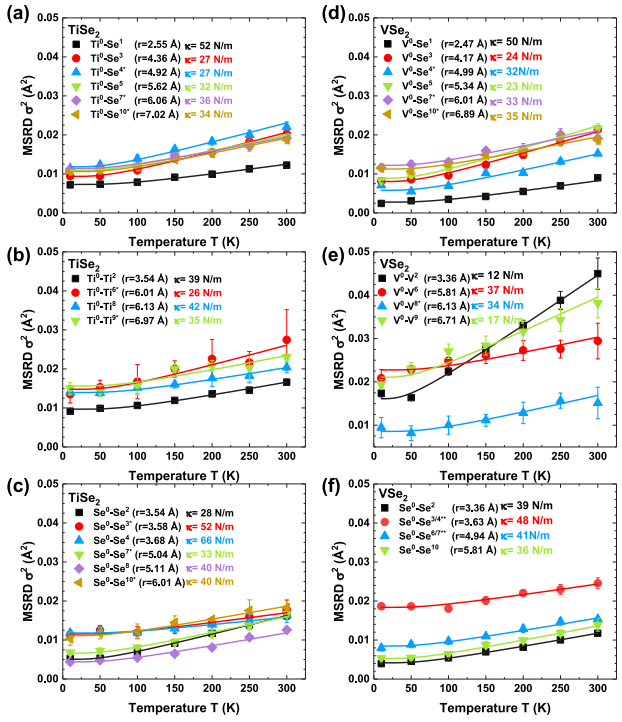

Fig. 7. Temperature dependence of the mean-square relative displacement (MSRD) factors σ^2 for Ti(V)–Se (a,d), Ti–Ti(V–V) (b,e), and Se–Se (c,f) atom pairs in $TiSe_2$ and VSe_2. Solid lines correspond to the fits using the correlated Einstein model [46]. Calculated values of the effective force constants κ are also given.

contribution from the first coordination shell composed of six selenium atoms. Contributions from distant coordination shells are also present up to 7 Å but they are relatively weaker. This fact contrasts with the Se K-edge EXAFS spectra where strong contributions from distant shells are observed in FTs up to 5 Å but appreciable signals are visible even at longer distances.

The results of the RMC/EA fits for VSe_2 are in good agreement with the experimental data at both V and Se K-edges (Fig. 4(b)). The partial RDFs for V–V, V–Se(Se–V), and Se–Se atom pairs are shown in Fig. 6(b), whereas the characteristic Einstein frequencies ω_E and the effective force constants κ for all coordination shells are reported in Table 2.

The RDFs obtained for both TMDs (Fig. 6) exhibit an expected temperature dependence: they become broadened at higher temperatures. At the same time, no peak splitting is observed for the nearest shells at low temperatures in the CDW state. This suggests that the expected lattice distortions due to atom displacements [10,19] are relatively small compared to thermal disorder effects. Nevertheless, upon comparing the partial RDFs for $TiSe_2$ and VSe_2, a notable difference in the temperature dependence between Ti–Ti and V–V RDFs is observed within the range of the second coordination shell. Upon increasing temperature, the V_0–V_2 RDF peak at 3.36 Å in VSe_2 becomes significantly more broadened compared to the Ti_0–Ti_2 RDF peak at 3.54 Å in $TiSe_2$. This difference is well reflected by the temperature dependence of respective MSRDs in Fig. 7(b) and (e). Indeed, the MSRD for the V_0–V_2 atom pair exhibits a rapid increase above 50 K, displaying anomalous behavior compared to MSRDs for other atom pairs. Note that the value of the force constant $\kappa_{V_0-V_2} \approx 12$ N/m is the smallest one (Table 2).

There is also a prominent difference in the splitting of the peak around 3.6 Å in the Se–Se RDFs between the two TMDs. A single peak at 3.55 Å is present in $TiSe_2$, whereas a double peak at about 3.35 Å and 3.68 Å exists in VSe_2. This difference is due to that the Se_0–Se_2 distance in VSe_2 is significantly shorter by 0.18 Å than in $TiSe_2$ (see Tables 1 and 2).

4. Conclusions

Highly crystalline bulk 1T-$TiSe_2$ and 1T-VSe_2 were synthesized using the chemical vapor transport technique, and their local atomic structure and lattice dynamics were studied by temperature-dependent (10–300 K) X-ray absorption spectroscopy at the Ti, V, and Se K-edges.

The extended X-ray absorption fine structure (EXAFS) spectra were analyzed using the reverse Monte Carlo (RMC) simulations [26,27] by a simultaneous fitting of metal (Ti/V) and selenium K-edge spectra

(Fig. 4). Such an approach allowed us to reconstruct the local environment in both selenides in terms of the partial radial distribution functions (Fig. 6) and to gain reliable information on disorder effects in the nearest and distant coordination shells. The mean-square relative displacements σ^2 for atom pairs located in the first ten coordination shells were determined, and their temperature dependencies were approximated using the correlated Einstein model. As a result, the characteristic Einstein frequencies ω_E and the effective force constants κ were obtained (Tables 1 and 2) for all atomic pairs and used in the assessment of the strengths of intralayer and interlayer interactions.

The partial RDFs obtained for both TMDs (Fig. 6) demonstrate the expected temperature dependence and do not show any evidence of the peak splitting for the nearest shells at low temperatures due to the CDW state. This indicates that CDW-induced atom displacements [10,19] are relatively small compared to thermal disorder effects. Nevertheless, a comparison of the RDFs for Ti–Ti and V–V atom pairs located within the same layer shows their different temperature variations. In particular, the thermal disorder significantly affects the V_0–V_2 atom pair as can be seen from the temperature dependence of its MSRD $\sigma^2_{V_0-V_2}$ (Fig. 7) and small value of the force constant $\kappa_{V_0-V_2} \approx 12$ N/m (Table 2).

Thus, the RMC/EA-EXAFS technique shows great potential for studying the local atomic structure and disorder effects in TMDs and other layered materials.

CRediT authorship contribution statement

Inga Pudza: Writing – review & editing, Writing – original draft, Visualization, Investigation. **Boris Polyakov:** Writing – review & editing, Writing – original draft, Investigation. **Kaspars Pudzs:** Investigation. **Edmund Welter:** Resources. **Alexei Kuzmin:** Writing – review & editing, Writing – original draft, Methodology, Investigation, Conceptualization.

Declaration of competing interest

The authors declare that they have no known competing financial interests or personal relationships that could have appeared to influence the work reported in this paper.

Data availability

Data will be made available on request.

Acknowledgments

B.P. and A.K. thank the support of the Latvian Council of Science, Latvia project No. LZP-2020/1-0261. The experiment at the PETRA III synchrotron was performed within proposal No. I-20210625 EC. The synchrotron experiment has been supported by the project CALIPSOplus under the Grant Agreement 730872 from the EU Framework Programme for Research and Innovation HORIZON 2020. Institute of Solid State Physics, University of Latvia as the Center of Excellence has received funding from the European Union's Horizon 2020 Framework Programme H2020-WIDESPREAD-01-2016-2017-TeamingPhase2 under grant agreement No. 739508, project CAMART2.

References

[1] G.R. Bhimanapati, Z. Lin, V. Meunier, Y. Jung, J. Cha, S. Das, D. Xiao, Y. Son, M.S. Strano, V.R. Cooper, et al., Recent advances in two-dimensional materials beyond graphene, ACS Nano 9 (2015) 11509–11539, http://dx.doi.org/10.1021/acsnano.5b05556.

[2] H. Zhan, D. Guo, G. Xie, Two-dimensional layered materials: from mechanical and coupling properties towards applications in electronics, Nanoscale 11 (2019) 13181–13212, http://dx.doi.org/10.1039/C9NR03611C.

[3] V. Shanmugam, R.A. Mensah, K. Babu, S. Gawusu, A. Chanda, Y. Tu, R.E. Neisiany, M. Försth, G. Sas, O. Das, A review of the synthesis properties, and applications of 2D materials, Part. Part. Syst. Charact. 39 (2022) 2200031, http://dx.doi.org/10.1002/ppsc.202200031.

[4] Y.-C. Lin, R. Torsi, R. Younas, C.L. Hinkle, A.F. Rigosi, H.M. Hill, K. Zhang, S. Huang, C.E. Shuck, C. Chen, et al., Recent advances in 2D material theory, synthesis, properties, and applications, ACS Nano 17 (2023) 9694–9747, http://dx.doi.org/10.1021/acsnano.2c12759.

[5] T. Ritschel, J. Trinckauf, K. Koepernik, B. Büchner, M.V. Zimmermann, H. Berger, Y. Joe, P. Abbamonte, J. Geck, Orbital textures and charge density waves in transition metal dichalcogenides, Nat. Phys. 11 (2015) 328–331, http://dx.doi.org/10.1038/nphys3267.

[6] M. Hossain, Z. Zhao, W. Wen, X. Wang, J. Wu, L. Xie, Recent advances in two-dimensional materials with charge density waves: synthesis, characterization and applications, Crystals 7 (2017) 298, http://dx.doi.org/10.3390/cryst7100298.

[7] W. Jolie, T. Knispel, N. Ehlen, K. Nikonov, C. Busse, A. Grueneis, T. Michely, Charge density wave phase of VSe_2 revisited, Phys. Rev. B 99 (2019) 115417, http://dx.doi.org/10.1103/PhysRevB.99.115417.

[8] J. Wilson, F. Di Salvo, S. Mahajan, Charge-density waves in metallic, layered, transition-metal dichalcogenides, Phys. Rev. Lett. 32 (1974) 882, http://dx.doi.org/10.1103/PhysRevLett.32.882.

[9] M. Leroux, L. Cario, A. Bosak, P. Rodiere, Traces of charge density waves in NbS_2, Phys. Rev. B 97 (2018) 195140, http://dx.doi.org/10.1103/PhysRevB.97.195140.

[10] Z. Guo, X. Hao, J. Dong, H. Li, J. Liao, D. Chen, Observation of pressure induced charge density wave order and eightfold structure in bulk VSe_2, Sci. Rep. 11 (2021) 18157, http://dx.doi.org/10.1038/s41598-021-97630-8.

[11] K. Rossnagel, On the origin of charge-density waves in select layered transition-metal dichalcogenides, J. Phys.: Condens. Matter 23 (2011) 213001, http://dx.doi.org/10.1088/0953-8984/23/21/213001.

[12] M. Adam, H. Zhu, Z. Liu, S. Cui, P. Zhang, Y. Liu, G. Zhang, X. Wu, Z. Sun, L. Song, Charge density wave phase suppression in 1T-$TiSe_2$ through Sn intercalation, Nano Res. 15 (2022) 2643–2649, http://dx.doi.org/10.1007/s12274-021-3859-0.

[13] C. Riekel, Structure refinement of $TiSe_2$ by neutron diffraction, J. Solid State Chem. 17 (1976) 389–392, http://dx.doi.org/10.1016/S0022-4596(76)80008-4.

[14] E. Hoschek, Vanadinselenide, Z. Anorg. Allg. Chem. 242 (1939) 49.

[15] Y. Liu, N. Weiss, X. Duan, H.-C. Cheng, Y. Huang, X. Duan, Van der Waals heterostructures and devices, Nat. Rev. Mater. 1 (2016) 16042, http://dx.doi.org/10.1038/natrevmats.2016.42.

[16] Z. Shi, X. Wang, Y. Sun, Y. Li, L. Zhang, Interlayer coupling in two-dimensional semiconductor materials, Semicond. Sci. Technol. 33 (2018) 093001, http://dx.doi.org/10.1088/1361-6641/aad6c3.

[17] R. Bian, C. Li, Q. Liu, G. Cao, Q. Fu, P. Meng, J. Zhou, F. Liu, Z. Liu, Recent progress in the synthesis of novel two-dimensional van der Waals materials, Natl. Sci. Rev. 9 (2021) nwab164, http://dx.doi.org/10.1093/nsr/nwab164.

[18] I. Pudza, D. Bocharov, A. Anspoks, M. Krack, A. Kalinko, E. Welter, A. Kuzmin, Unraveling the interlayer and intralayer coupling in two-dimensional layered MoS_2 by X-ray absorption spectroscopy and ab initio molecular dynamics simulations, Mater. Today Commun. 35 (2023) 106359, http://dx.doi.org/10.1016/j.mtcomm.2023.106359.

[19] F.J. Di Salvo, D.E. Moncton, J.V. Waszczak, Electronic properties and superlattice formation in the semimetal $TiSe_2$, Phys. Rev. B 14 (1976) 4321–4328, http://dx.doi.org/10.1103/PhysRevB.14.4321.

[20] M. Holt, P. Zschack, H. Hong, M.Y. Chou, T.-C. Chiang, X-ray studies of phonon softening in $TiSe_2$, Phys. Rev. Lett. 86 (2001) 3799–3802, http://dx.doi.org/10.1103/PhysRevLett.86.3799.

[21] F. Weber, S. Rosenkranz, J.-P. Castellan, R. Osborn, G. Karapetrov, R. Hott, R. Heid, K.-P. Bohnen, A. Alatas, Electron–phonon coupling and the soft phonon mode in $TiSe_2$, Phys. Rev. Lett. 107 (2011) 266401, http://dx.doi.org/10.1103/PhysRevLett.107.266401.

[22] M. Bayard, M. Sienko, Anomalous electrical and magnetic properties of vanadium diselenide, J. Solid State Chem. 19 (1976) 325–329, http://dx.doi.org/10.1016/0022-4596(76)90184-5.

[23] D. Eaglesham, R. Withers, D. Bird, Charge-density-wave transitions in 1T-VSe_2, J. Phys. C: Solid State Phys. 19 (1986) 359, http://dx.doi.org/10.1088/0022-3719/19/3/006.

[24] J. Diego, A.H. Said, S.K. Mahatha, R. Bianco, L. Monacelli, M. Calandra, F. Mauri, K. Rossnagel, I. Errea, S. Blanco-Canosa, van der Waals driven anharmonic melting of the 3D charge density wave in VSe_2, Nature Commun. 12 (2021) 598, http://dx.doi.org/10.1038/s41467-020-20829-2.

[25] J. Feng, R.A. Susilo, B. Lin, W. Deng, Y. Wang, B. Li, K. Jiang, Z. Chen, X. Xing, Z. Shi, C. Wang, B. Chen, Achieving room-temperature charge density wave in transition metal dichalcogenide 1T-VSe_2, Adv. Electron. Mater. 6 (2020) 1901427, http://dx.doi.org/10.1002/aelm.201901427.

[26] J. Timoshenko, A. Kuzmin, J. Purans, Reverse Monte Carlo modeling of thermal disorder in crystalline materials from EXAFS spectra, Comp. Phys. Commun. 183 (2012) 1237–1245, http://dx.doi.org/10.1016/j.cpc.2012.02.002.

[27] J. Timoshenko, A. Kuzmin, J. Purans, EXAFS study of hydrogen intercalation into ReO_3 using the evolutionary algorithm, J. Phys.: Condens. Matter 26 (2014) 055401, http://dx.doi.org/10.1088/0953-8984/26/5/055401.

[28] R.L. McGreevy, L. Pusztai, Reverse Monte Carlo simulation: a new technique for the determination of disordered structures, Mol. Simul. 1 (1988) 359–367, http://dx.doi.org/10.1080/08927028808080958.

[29] S.J. Gurman, R.L. McGreevy, Reverse Monte Carlo simulation for the analysis of EXAFS data, J. Phys.: Condens. Matter 2 (1990) 9463, http://dx.doi.org/10.1088/0953-8984/2/48/001.

[30] Y. Kubo, N. Ishimatsu, N. Kitamura, N. Kawamura, S. Kakizawa, M. Mizumaki, R. Nomura, T. Irifune, H. Sumiya, Visualization of the disordered structure of Fe-Ni invar alloys by reverse monte carlo calculations, Front. Mater. 9 (2022) 954110, http://dx.doi.org/10.3389/fmats.2022.954110.

[31] J.C. Woicik, E. Cockayne, E.L. Shirley, I. Levin, C. Weiland, B. Ravel, A.M.M. Abeykoon, Lattice vibrations and energy landscape of the isoelectronic semiconductor series CuBr, ZnSe, GaAs, and Ge: The special case of CuBr and its *d*-level chemistry, Phys. Rev. B 108 (2023) 195202, http://dx.doi.org/10.1103/PhysRevB.108.195202.

[32] M. Winterer, J. Geiß, Combining reverse Monte Carlo analysis of X-ray scattering and extended X-ray absorption fine structure spectra of very small nanoparticles, J. Appl. Crystallogr. 56 (2023) 103–109, http://dx.doi.org/10.1107/S1600576722010858.

[33] C. Liu, Z. Zhang, J. Ding, E. Ma, On the reliability of using reverse Monte Carlo simulations to construct the atomic structure model of metallic glasses, Scr. Mater. 225 (2023) 115159, http://dx.doi.org/10.1016/j.scriptamat.2022.115159.

[34] A. Di Cicco, F. Iesari, Advances in modelling X-ray absorption spectroscopy data using reverse Monte Carlo, Phys. Chem. Chem. Phys. 24 (2022) 6988–7000, http://dx.doi.org/10.1039/D1CP05525A.

[35] A. Ubaldini, E. Giannini, Improved chemical vapor transport growth of transition metal dichalcogenides, J. Cryst. Growth 401 (2014) 878–882, http://dx.doi.org/10.1016/j.jcrysgro.2013.12.070.

[36] J. Pandey, A. Soni, Electron–phonon interactions and two-phonon modes associated with charge density wave in single crystalline 1T-VSe_2, Phys. Rev. Res. 2 (2020) 033118, http://dx.doi.org/10.1103/PhysRevResearch.2.033118.

[37] E. Welter, R. Chernikov, M. Herrmann, R. Nemausat, A beamline for bulk sample x-ray absorption spectroscopy at the high brilliance storage ring PETRA III, AIP Conf. Proc. 2054 (2019) 040002, http://dx.doi.org/10.1063/1.5084603.

[38] A. Kuzmin, J. Chaboy, EXAFS and XANES analysis of oxides at the nanoscale, IUCrJ 1 (2014) 571–589, http://dx.doi.org/10.1107/S2052252514021101.

[39] A. Kalinko, 2023, XAESAv0.07.

[40] A.L. Ankudinov, B. Ravel, J.J. Rehr, S.D. Conradson, Real-space multiple-scattering calculation and interpretation of x-ray-absorption near-edge structure, Phys. Rev. B 58 (1998) 7565–7576, http://dx.doi.org/10.1103/PhysRevB.58.7565.

[41] J.J. Rehr, R.C. Albers, Theoretical approaches to x-ray absorption fine structure, Rev. Mod. Phys. 72 (2000) 621–654, http://dx.doi.org/10.1103/RevModPhys.72.621.

[42] L. Hedin, B.I. Lundqvist, Explicit local exchange–correlation potentials, J. Phys. C: Solid State Phys. 4 (1971) 2064, http://dx.doi.org/10.1088/0022-3719/4/14/022.

[43] F.R. Hampel, Robust estimation: A condensed partial survey, Z. Wahrscheinlichkeit. 27 (1973) 87–104, http://dx.doi.org/10.1007/BF00536619.

[44] M. Daszykowski, K. Kaczmarek, Y. Vander Heyden, B. Walczak, Robust statistics in data analysis–A review: Basic concepts, Chemom. Intell. Lab. Syst. 85 (2007) 203–219, http://dx.doi.org/10.1016/j.chemolab.2006.06.016.

[45] J. Timoshenko, A. Kuzmin, Wavelet data analysis of EXAFS spectra, Comp. Phys. Commun. 180 (2009) 920–925, http://dx.doi.org/10.1016/j.cpc.2008.12.020.

[46] E. Sevillano, H. Meuth, J. Rehr, Extended x-ray absorption fine structure Debye–Waller factors. I. Monatomic crystals, Phys. Rev. B 20 (1979) 4908, http://dx.doi.org/10.1103/PhysRevB.20.4908.

[47] G. Dalba, P. Fornasini, EXAFS Debye–Waller factor and thermal vibrations of crystals, J. Synchrotron Radiat. 4 (1997) 243–255, http://dx.doi.org/10.1107/S0909049597006900.

[48] A. Kuzmin, J. Timoshenko, A. Kalinko, I. Jonane, A. Anspoks, Treatment of disorder effects in x-ray absorption spectra beyond the conventional approach, Radiat. Phys. Chem. 175 (2020) 108112, http://dx.doi.org/10.1016/j.radphyschem.2018.12.032.